Inhibiting collective cation migration in Li-rich cathode materials as a strategy to mitigate voltage hysteresis

Jianping Huang [1,5], Bin Ouyang [1,2,5], Yaqian Zhang [1,2], Liang Yin [3], Deok-Hwang Kwon [1,2], Zijian Cai [1,2], Zhengyan Lun [1,2], Guobo Zeng [2], Mahalingam Balasubramanian [4] & Gerbrand Ceder [1,2] ✉

Lithium-rich cathodes are promising energy storage materials due to their high energy densities. However, voltage hysteresis, which is generally associated with transition metal migration, limits their energy efficiency and implementation in practical devices. Here we reveal that voltage hysteresis is related to the collective migration of metal ions, and that isolating the migration events from each other by creating partial disorder can create high-capacity reversible cathode materials, even when migrating transition metal ions are present. We demonstrate this on a layered Li-rich chromium manganese oxide that in its fully ordered state displays a substantial voltage hysteresis (>2.5 V) associated with collective transition metal migration into Li layers, but can be made to achieve high capacity (>360 mAh g^{-1}) and energy density (>1,100 Wh kg^{-1}) when the collective migration is perturbed by partial disorder. This study demonstrates that partially cation-disordered cathode materials can accommodate a high level of transition metal migration, which broadens our options for redox couples to those of mobile cations.

Rechargeable Li-ion batteries have been widely applied in consumer electronics and electric vehicles[1,2]. The rapidly increasing demand for long-range electric vehicles demands Li-ion batteries with high energy density and low cost. High capacity in cathodes requires the combination of high cyclable Li content with good Li diffusion kinetics, high electron redox capacity and high stability even under large changes in Li content and metal valence. These requirements are often in conflict with each other, as exemplified by Li-rich oxides, a promising category of high-capacity cathodes. Because of their high Li content, they have less transition metal (TM) capacity and contain less well hybridized oxygen[3], which both lead to greater reliance on oxygen redox. This in turn tends to decrease stability and creates more pronounced hysteresis. For example, layered Li-rich TM oxides (that is, Li$_{1+x}$Ni$_y$Co$_x$Mn$_{1-x-y-z}$O$_2$) have large capacities (>250 mAh g^{-1}) but show voltage hysteresis and continuous voltage fade[4]. Recently proposed mechanisms for this hysteresis involve oxygen oxidation, TM migration[5,6] and oxidation of O^{2-} to molecular O$_2$ that is then trapped in the bulk[6].

In principle, Li-rich materials that use ions with multiple redox couples (for example, Cr^{3+}/Cr^{6+}, V^{3+}/V^{5+} and Mo^{3+}/Mo^{6+}) can remove the trade-off between Li excess and transition metal capacity, and thereby reduce oxygen redox[7,8]. Some efforts to find high-energy cathodes in this space in the past have focused on systems with very high theoretical capacity (>300 mAh g^{-1}) such as xLi$_2$MnO$_3$•(1 − x) LiCrO$_2$ (refs. [7–11]) and xLi$_2$TiO$_3$•(1 − x)LiCrO$_2$ (refs. [12–15]). However, in practice Li$_{1.22}$Cr$_{0.33}$Mn$_{0.45}$O$_2$ only delivers a reversible capacity of about 130 mAh g^{-1} with a large irreversible capacity (~90 mAh g^{-1}) between 2.0 and 4.35 V, which Dahn et al. attributed to the irreversible migration of Cr from the TM layer to the Li layer[10,11]. These examples illustrate the

[1]Materials Sciences Division, Lawrence Berkeley National Laboratory, Berkeley, CA, USA. [2]Department of Materials Science and Engineering, University of California, Berkeley, CA, USA. [3]X-ray Science Division, Advanced Photon Source, Argonne National Laboratory, Argonne, IL, USA. [4]Electrification and Energy Infrastructures Division, Oak Ridge National Laboratory, Oak Ridge, TN, USA. [5]These authors contributed equally: Jianping Huang, Bin Ouyang. ✉e-mail: gceder@berkeley.edu
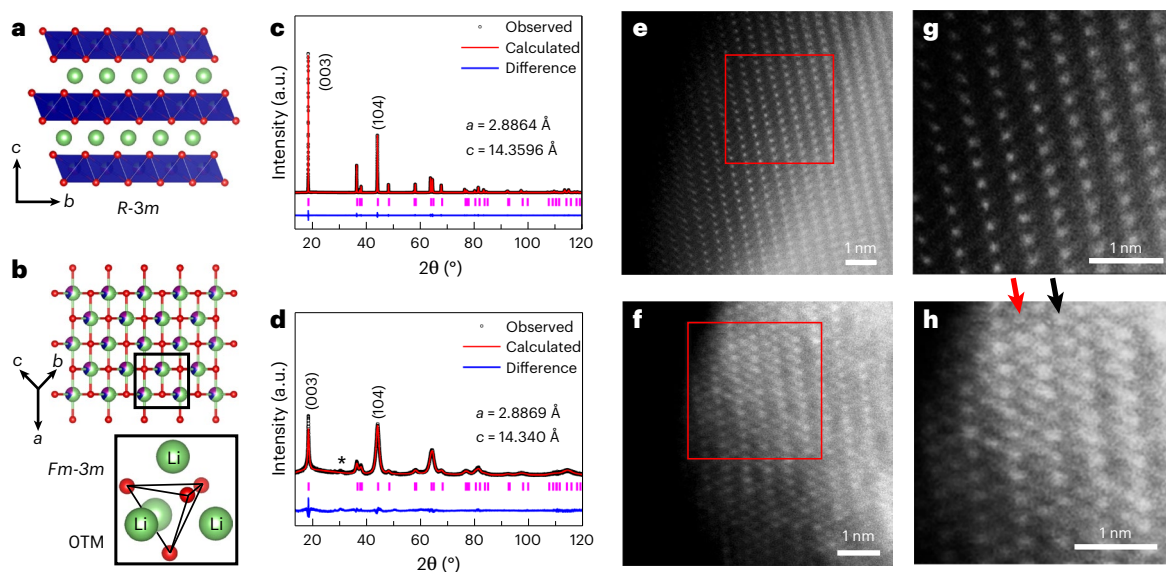
Fig. 1 | Structure characterization of L-LCMO and PD-LCMO. a,b, Crystal structures of L-LCMO (**a**) and PD-LCMO (**b**). Li, Cr, Mn and O are shown in green, blue, purple and red, respectively. The inset in **b** shows a tetrahedral site face-shared by four Li atoms and zero TM atoms (0TM site). **c,d,** Synchrotron XRD patterns and refinement results for L-LCMO (**c**) and PD-LCMO (**d**). Bragg positions are indicated by the vertical pink bars. The asterisk in **d** indicates zirconium oxide introduced in the ball milling process. **e–h,** High-resolution HAADF-STEM images of L-LCMO (**e,g**) and PD-LCMO (**f,h**) PD-LCMO along the [010] zone axis. The red boxes in **e** and **f** indicate the regions shown in **g** and **h**, respectively. A decreased Z-contrast difference between the Li column and Li–Cr–Mn column is observed in (**f**) and (**h**), indicating cation mixing. The red arrow in **h** highlights a high degree of cation mixing in the Li column, whereas the black arrow highlights a lower degree of cation mixing. a.u., arbitrary units.

more general challenge in cathode design: either one uses immobile ions in ordered cathodes, which limits the redox active elements in the layered structure to Ni and Co, hence the lithium nickel manganese cobalt oxide (NMC) class, or one uses ions that can migrate during electrochemical cycling and deals with hysteresis and/or capacity/voltage fade due to structural changes.

To mitigate the hysteretic effect induced by TM migration, a general strategy is to minimize the opportunity for cation disorder during electrochemical cycling. For example, Kang et al. limited cation disorder by restricting TM migration to the Li layer using an O_2-type $Li_x(Li_{0.2}Ni_{0.2}Mn_{0.6})O_2$ ($x \approx 0.83$). In this structure, occupation of a TM in a Li site is destabilized by the strong electrostatic repulsion it experiences from the TM layer. Such structural engineering was found to reduce irreversible TM migration, as well as voltage hysteresis[16].

In this work we propose an alternative strategy that allows TM migration but creates enough disorder that the TM migration cannot occur collectively, thereby minimizing hysteresis. We demonstrate that introducing cation disorder in layered Li-rich $Li_{1.2}Cr_{0.4}Mn_{0.4}O_2$ (L-LCMO) effectively mitigates voltage hysteresis and increases the reversibility of the Cr^{3+}/Cr^{6+} redox couple. $Li_{1.2}Cr_{0.4}Mn_{0.4}O_2$ with partial cation disorder (PD-LCMO) shows a large reversible capacity of >200 mAh g^{-1} for 100 cycles at 100 mA g^{-1} due to the inhibited collective Cr migration. The successful manipulation of reversible multi-electron redox and TM migration through partial redox active element cation disordering provides opportunities to realize high-performance cathode materials for Li-ion batteries.

Characterization of layered and disordered $Li_{1.2}Cr_{0.4}Mn_{0.4}O_2$

We compare in this work fully ordered (Fig. 1a), fully disordered (Fig. 1b) and partially disordered samples. Cation disorder was introduced into L-LCMO through shear stress induced by mechanical milling[17,18]; this sample exhibited partial cation mixing and is denoted PD-LCMO. L-LCMO was synthesized using a solid-state method in a structure that could be indexed to the *R-3m* space group using synchrotron X-ray

diffraction (XRD; Fig. 1c). No diffraction peak was observed in the 2θ region of 20–30°, indicating the absence of Li_2MnO_3-like domains. The refined lattice parameters *a* and *c* were 2.8864 Å and 14.3596 Å, respectively, similar to previously reported values[8–10]. The *c/a* ratio, which can be used as a measure of 'layeredness', of L-LCMO was 4.97, which is close to that of $LiCoO_2$ (4.99)[9]. The PD-LCMO was prepared by mechanical milling of the L-LCMO for 1 h. The ball milling caused the relative intensity of the (003) diffraction peak to decrease, suggesting a more disordered structure, as shown in Fig. 1d. The results of joint XRD and neutron diffraction refinement indicate ~18% cation mixing in PD-LCMO (Supplementary Table 1 and Supplementary Fig. 1). Direct evidence of disordering was further confirmed by aberration-corrected high-angle-annular-dark-field scanning transmission electron microscopy (HAADF-STEM) shown in Fig. 1e–h. The *Z*-contrast high-resolution STEM images (Fig. 1e,g) show stacking of Li and TM layers in L-LCMO, consistent with the XRD results. A decreased *Z*-contrast difference between the Li and TM layers was observed in PD-LCMO (Fig. 1f,h), indicating the presence of TM cations in the Li layer. The HAADF-STEM images of PD-LCMO indicate that some Li layers exhibit a high degree of cation mixing while others exhibit a lower degree of cation mixing. The fast Fourier transform pattern confirms the *R-3m* space group in PD-LCMO (Supplementary Fig. 2). These findings support the idea that the cation arrangement is partially disordered in PD-LCMO.

Electrochemistry

The voltage profiles of L-LCMO and PD-LCMO at 20 mA g^{-1} in the voltage window of 4.8–1.5 V are compared in Fig. 2a. L-LCMO delivered a discharge capacity of 297 mAh g^{-1} with two distinct voltage plateaus at approximately 3.6 and 1.6 V. Because 48% of the discharge capacity was delivered in the low-voltage (1.6 V) plateau, L-LCMO has a discharge energy density of only 770 Wh kg^{-1} with an average voltage of 2.6 V. This low discharge voltage plateau was also observed in a previous report on layered $Li_{1.2}Cr_{0.4}Mn_{0.4}O_2$ (ref. [8]). L-LCMO maintained the low discharge voltage plateau upon electrochemical cycling (Supplementary Fig. 3). PD-LCMO delivered an initial discharge capacity
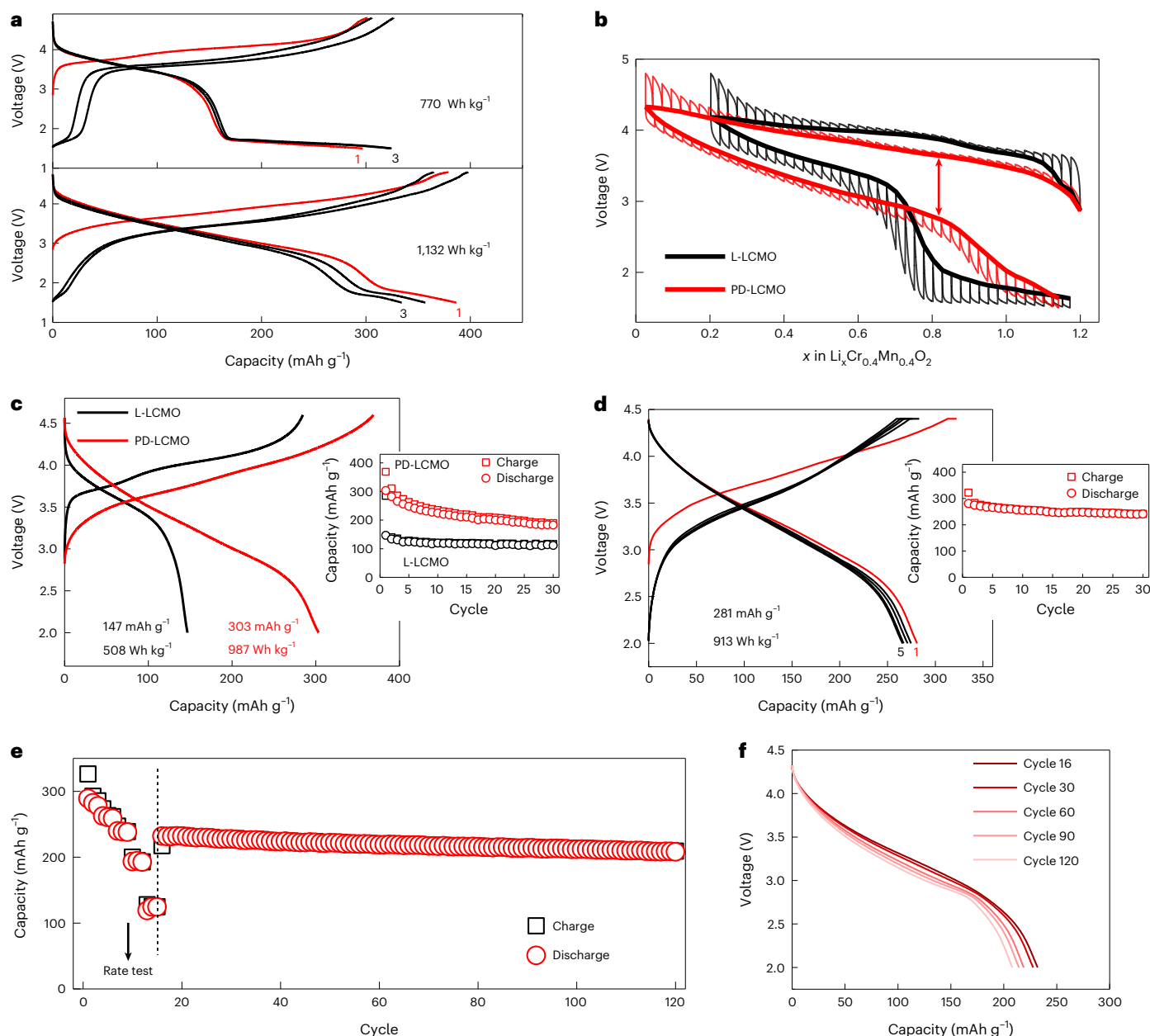
Fig. 2 | Electrochemistry of LCMO samples at room temperature. a, Voltage profiles of L-LCMO (top) and PD-LCMO (bottom) at 20 mA g⁻¹ in a voltage window of 4.8–1.5 V from cycle 1 to cycle 3. The voltage profiles of cycle 1 are plotted as red lines and labeled as 1 in red. The voltage profiles of cycle 2 and 3 are plotted as black lines, and the number 3 in black labels the voltage profiles of cycle 3. **b,** Voltage profiles of L-LCMO and PD-LCMO measured under the galvanostatic intermittent titration technique mode. The quasi-equilibrium voltages are plotted as thick lines, and the voltage profiles are plotted as thin lines. The red arrow indicates the voltage hysteresis. **c,** First-cycle voltage profiles (left) and capacity retention (right) of L-LCMO and PD-LCMO at 20 mA g⁻¹ in a voltage window of 4.6–2.0 V. The numbers indicate the capacity and energy density of L-LCMO (black) and PD-LCMO (red). **d,** Voltage profiles (left) and capacity retention (right) of PD-LCMO in a voltage window of 4.4–2.0 V. The voltage

profiles of cycle 1 are plotted as red lines and labeled as 1 in red. The voltage profiles of cycles 2–5 are plotted as black lines, and the number 5 in black labels the voltage profiles of cycle 5. The first-cycle capacity and energy density of PD-LCMO are shown in **d.** The test was performed under constant-current constant-voltage charging mode by charging the cell at 20 mA g⁻¹ to 4.4 V and holding at 4.4 V for 1 h. Lithium bis(fluorosulfonyl)amide (LiFSI):dimethyl carbonate (DMC) in a molar ratio of 1:1.1 was used as the electrolyte. **e,** Capacity retention of PD-LCMO at different current densities. The rate capability test was performed at 20, 50, 100, 200 and 500 mA g⁻¹ for three cycles, respectively (cycles 1–15), and the long cycle stability test was performed at 100 mA g⁻¹ (cycles 16–120) in a voltage window of 4.4–2.0 V. **f,** Discharge voltage profiles of PD-LCMO from cycle 16 to cycle 120 in **e.**

of 387 mAh g⁻¹ (1.2 Li⁺). Notably, 79% of the discharge capacity was delivered above 2 V for PD-LCMO, leading to a high discharge energy density of 1,132 Wh kg⁻¹.

The voltage hysteresis and polarization were analysed using galvanostatic intermittent titration (Fig. 2b). While both L-LCMO and PD-LCMO exhibited voltage hysteresis in the quasi-equilibrium voltage

curves, this hysteresis was twice as large for L-LCMO with a composition of $Li_{0.8}Cr_{0.4}Mn_{0.4}O_2$. The presence of the voltage hysteresis in the quasi-equilibrium voltage curves suggests that it is created by a quasi-thermodynamic effect, rather than by basic Li⁺ or e⁻ transport limitations. Reduced polarization could also be observed in PD-LCMO during the discharge process (Supplementary Fig. 4).
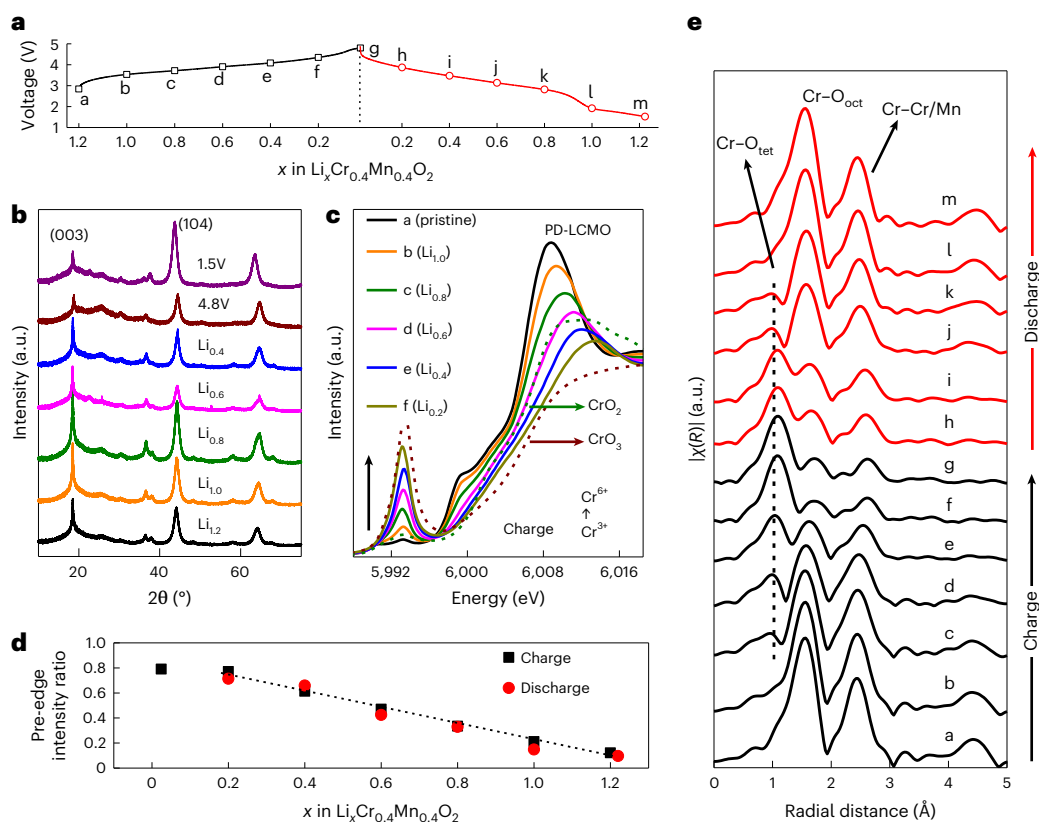
Fig. 3 | Redox mechanism and structural change in PD-LCMO. a, Voltage profile of PD-LCMO at 20 mA g^{-1} with symbols indicating the compositions of the ex situ PD-LCMO samples. The dashed black line shows the end of charge and the beginning of discharge. **b,** Synchrotron XRD patterns of PD-LCMO at different states of charge and discharge. **c,** Cr K-edge XANES spectra of PD-LCMO upon delithiation. The spectra of the CrO_2 and CrO_3 standards are plotted as dashed lines. The black arrow shows that the pre-edge intensity increases in the charge process. **d,** Pre-edge intensity ratio of $Li_xCr_{0.4}Mn_{0.4}O_2$ and the CrO_3 standard. The dashed black line shows that the relationship between lithium content and pre-edge intensity ratio follows a linear trend. **e,** Cr K-edge EXAFS of PD-LCMO upon delithiation and lithiation. The peaks at ~1.0, ~1.5 and ~2.5 Å correspond to the tetrahedral Cr–O (Cr–O$_{tet}$), octahedral Cr–O (Cr–O$_{oct}$) and Cr–Cr/Mn coordinations, respectively. |χ(R)|, magnitude of Fourier transformed EXAFS.

The reduced voltage hysteresis and polarization in PD-LCMO contributed to the high reversible capacity above 2.0 V. PD-LCMO delivered a discharge capacity of 303 mAh g^{-1} (987 Wh kg^{-1}) in a voltage window of 4.6–2.0 V (Fig. 2c), which is comparable to or higher than that of current promising high-energy cathode materials under similar test conditions—that is, disordered Li_2MnO_2F (283 mAh g^{-1}, 960 Wh kg^{-1})[19], layered $Li_{1.2}Ni_{0.13}Mn_{0.54}Co_{0.13}O_2$ (~270 mAh g^{-1}, ~950 Wh kg^{-1})[20] and disordered $Li_2Mn_{0.5}Ti_{0.5}O_2F$ (237 mAh g^{-1}, 767 Wh kg^{-1})[21]. In contrast, L-LCMO delivered a discharge capacity of only 147 mAh g^{-1} in a voltage window of 4.6–2.0 V. PD-LCMO showed a superior rate capability between 4.4 and 2.0 V with a delivered capacity of 222 mAh g^{-1} at 500 mA g^{-1}, which is higher than current promising Li-rich cathode materials (Supplementary Fig. 5 and Supplementary Table 2). To determine the long-term cycling stability, PD-LCMO was cycled in a voltage window of 4.4–2.0 V using a concentrated electrolyte (LiFSI:DMC in a molar ratio of 1:1.1) (Fig. 2d–f). PD-LCMO maintained a reversible capacity >240 mAh g^{-1} at 20 mA g^{-1} for 30 cycles, exhibiting higher cycling stability than that in the 1 M LiPF$_6$ electrolyte (Supplementary Fig. 6), which can be attributed to reduced TM dissolution (Supplementary Fig. 7)[22,23]. PD-LCMO showed a reasonable rate capability with a capacity of 128 mAh g^{-1} at 500 mA g^{-1}, although the high viscosity of the concentrated electrolyte probably limited Li kinetics[24,25]. After the rate test, PD-LCMO was cycled at 100 mA g^{-1} from cycle 16 to cycle 120. The discharge capacity slightly decreased from 232 to 208 mAh g^{-1} with <0.1% fade per cycle, and the average discharge voltage showed minor fade (0.05 V) from cycle 16 to cycle 120.

Redox mechanism and structural change

The relative intensity of the (003) diffraction peak in PD-LCMO gradually reduced upon charging to 4.8 V, suggesting the loss of some layered-like order (Fig. 3b). When PD-LCMO was charged from the pristine state to the 4.8 V-charged state, the refined c lattice parameter decreased from 14.35 to 14.22 Å, and the unit cell showed a small volume decrease of 2.4% (Supplementary Fig. 8). Some peaks related to the layered structure at 48°, 58° and 68° disappeared in the XRD patterns of the 4.8 V-charged and 1.5 V-discharged samples, which indicates that Cr migration had occurred in the structure. Cr K-edge X-ray absorption near edge structure (XANES) spectroscopy was used to analyse the Cr redox (Fig. 3c). The Cr edge energy gradually shifted from 5,998 to 6,005 eV upon delithiation (from a to f), indicative of Cr^{3+} oxidation. A prominent pre-edge at ~5,993 eV appeared after delithiation, which is attributed to the formation of tetrahedral Cr^{6+}O$_4$ (Supplementary Note 1)[7]. Delithiating $Li_{1.2}Cr_{0.4}Mn_{0.4}O_2$ to $Li_{0.8}Cr_{0.4}Mn_{0.4}O_2$ is expected to lead to a nominal Cr^{4+} state. But the pre-edge peak in the spectrum of $Li_{0.8}Cr_{0.4}Mn_{0.4}O_2$ was more intense than that in the CrO$_2$ spectrum (Supplementary Fig. 9a), indicating that some tetrahedral Cr^{6+} was already present in $Li_{0.8}Cr_{0.4}Mn_{0.4}O_2$ (PD-LCMO). The pre-edge intensity ratio of $Li_{0.2}Cr_{0.4}Mn_{0.4}O_2$ and CrO$_3$, which can be utilized to determine the Cr^{6+} content in $Li_xCr_{0.4}Mn_{0.4}O_2$ (refs. [7,26,27]), was 0.77, indicating that Cr^{3+}/Cr^{6+} oxidation was the dominant oxidation process in the delithiation (Fig. 3d). Upon discharge, the pre-edge intensity continued to decrease, and the XANES spectrum at 1.5 V was similar to that of the pristine state (Supplementary Fig. 9). Mn reduction was not observed above 2.0 V,

but was observed to occur upon discharge to 1.5 V (see Supplementary Note 2 for Mn-edge XANES and Supplementary Fig. 10).

The local structural changes in PD-LCMO upon delithiation/lithiation were characterized using extended X-ray absorption fine structure (EXAFS) spectroscopy (Fig. 3e). In the charge process (from a to g), a new peak at ~1.0 Å appeared, which can be attributed to the short Cr–O bond (Cr–O$_{tet}$) in the tetrahedral site. The appearance of a tetrahedral Cr (Cr$_{tet}$) signature is consistent with the decreasing amplitude of the Cr–O$_{oct}$ peak, indicating that the Cr occupancy in the octahedral sites decreased. In the discharge process (from g to m), the amplitude of the Cr–O$_{tet}$ peak in the EXAFS spectra gradually faded, whereas that of the Cr–O$_{oct}$ peak increased. The EXAFS spectrum of the discharged PD-LCMO (1.5 V) was very similar to that of the pristine PD-LCMO, indicating recovery of the Cr coordination environment (Supplementary Fig. 11). The changes in the EXAFS spectra indicate that Cr migrates from an octahedral to a tetrahedral site upon charging and reversibly migrates back upon discharging.

To compare PD-LCMO with L-LCMO we also analysed the redox activity of Cr in L-LCMO using Cr K-edge XANES spectroscopy (Fig. 4b and Supplementary Fig. 12). The pre-edge region at ~5,993 eV of charged Li$_{0.8}$Cr$_{0.4}$Mn$_{0.4}$O$_2$ was similar to that of the CrO$_2$ standard. The absence of the prominent pre-edge peak in the Li$_{0.8}$Cr$_{0.4}$Mn$_{0.4}$O$_2$ XANES spectrum indicates that very little tetrahedral Cr^{6+} was present. The estimated Cr^{6+} contents at various stages of charge and discharge are summarized in Fig. 4c. During the charging process, 18% of Cr was oxidized to Cr^{6+} for a composition of Li$_{0.8}$Cr$_{0.4}$Mn$_{0.4}$O$_2$, which is smaller than the 33% in PD-LCMO of the same composition. Note that there would be 67% Cr^{3+} and 33% Cr^{6+} in Li$_{0.8}$Cr$_{0.4}$Mn$_{0.4}$O$_2$ if all redox occurred by three-electron Cr^{3+}/Cr^{6+} oxidation. Therefore, it seems that in L-LCMO Cr^{3+} is first oxidized to Cr^{4+} and then to Cr^{6+} upon charging. During the discharging process, the Cr^{6+} content linearly decreased, suggesting reduction of Cr^{6+} to Cr^{3+}. The different Cr^{6+} content at high Li concentrations ($x \geq 0.8$ in Li$_x$Cr$_{0.4}$Mn$_{0.4}$O$_2$) in the charging and discharging processes indicates hysteretic Cr redox in L-LCMO. Cr K-edge EXAFS spectroscopy confirmed irreversible Cr–O bond evolution upon charging/discharging (Supplementary Fig. 13).

The XRD patterns of L-LCMO at various stages of charge and discharge were collected to analyse the bulk structural change (Fig. 4d and Supplementary Fig. 14). The (003) diffraction peaks of the L-LCMO samples as shown in Fig. 4d indicate that the structure does not trace the same path during charge as during discharge. The *c* lattice parameter increased from 14.34 to 14.43 Å upon initial charging ($x \geq 0.8$ in Li$_x$Cr$_{0.4}$Mn$_{0.4}$O$_2$) and then decreased to 14.26 Å after charging to 4.8 V (Fig. 4e). Upon discharge, *c* increased from 14.26 to 14.33 Å at Li$_{0.4}$Cr$_{0.4}$Mn$_{0.4}$O$_2$ and then remained at approximately 14.33 Å up to discharge to 1.5 V. The irreversible lattice parameter change in L-LCMO seems to be related to a process at high Li concentration ($x \geq 0.8$ in Li$_x$Cr$_{0.4}$Mn$_{0.4}$O$_2$) and is consistent with the irreversible Cr–O bond distance change (Supplementary Fig. 13).

Cr migration in disordered and layered structures

The EXAFS spectra were fitted to obtain quantitative Cr coordination information (Fig. 5a, Supplementary Fig. 15 and Supplementary Tables 3 and 4). In PD-LCMO, the Cr$_{tet}$ content linearly increased to 65($\pm$3)% at the top of charge (Li$_{0.2}$Cr$_{0.4}$Mn$_{0.4}$O$_2$) and reversibly decreased to 0 upon discharging to 1.5 V. However, the Cr$_{tet}$ content in L-LCMO showed an irreversible change after one charge and discharge. For $x > 0.8$ in Li$_x$Cr$_{0.4}$Mn$_{0.4}$O$_2$, the amount of Cr$_{tet}$ in the charged state (0–13%) was consistently below that in the discharge state (0–25%). To investigate the preference for Cr migration in layered and disordered structures, the site energy difference ($E_{Tet} - E_{Oct}$) calculated using density functional theory for Cr was used to quantify the tendency of Cr migration in each structure (Fig. 5b). TM migration to a tetrahedral site requires that the face-sharing octahedral sites of this tetrahedral site are empty[28], which can be satisfied if a Li tri-vacancy forms in a
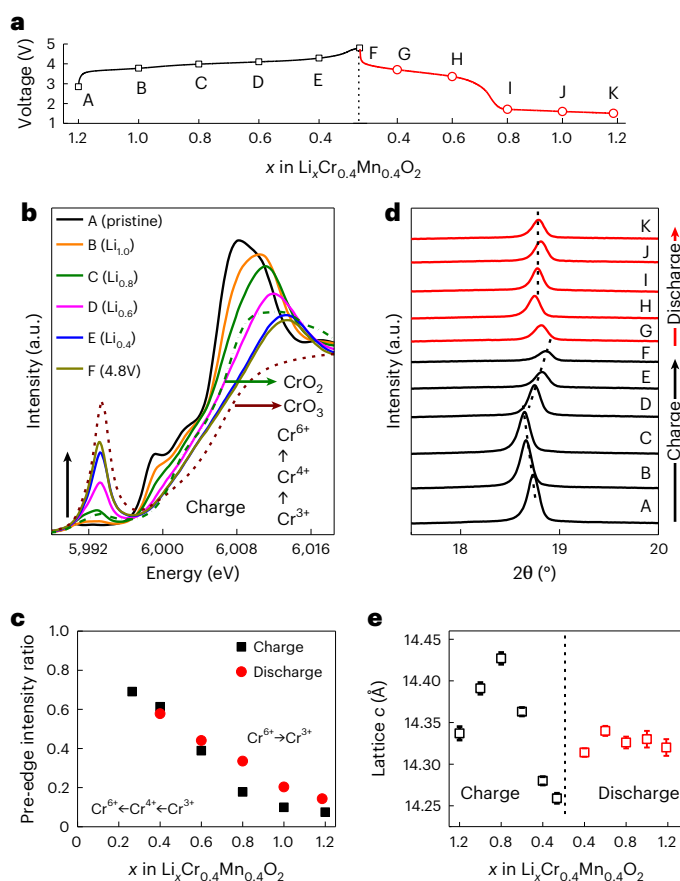

Fig. 4 | Redox mechanism and structural change in L-LCMO. a, Voltage profile of L-LCMO at 20 mA g^{-1} with symbols indicating the compositions of the ex situ L-LCMO samples. The dashed black line shows the end of charge and the beginning of discharge. **b**, Cr K-edge XANES spectra of L-LCMO upon delithiation. The spectra of the CrO$_2$ and CrO$_3$ standards are plotted as dashed lines. **c**, Pre-edge intensity ratio of Li$_x$Cr$_{0.4}$Mn$_{0.4}$O$_2$ and the CrO$_3$ standard. The black arrow shows that the pre-edge intensity increases in the charge process. **d**, XRD patterns around the (003) peak of ex situ L-LCMO samples at different delithiation/lithiation levels. The dashed black lines show the shift directions of the diffraction peak. The diffraction peak shifts to a lower 2θ value (from A to C) and then to a higher 2θ value (from C to F) upon charging. Upon discharging, the diffraction peak shifts to a lower 2θ value (from F to H) in the initial lithiation process and then remains at similar 2θ values (from H to K). **e**, Refined *c* lattice parameter in Li$_x$Cr$_{0.4}$Mn$_{0.4}$O$_2$. The error bars indicate the standard deviation of the *c* lattice parameter based on Rietveld refinement. The dashed black line separates the charge and discharge regions.

Li$_3$Cr tetrahedron. Thus, we removed all three Li ions in a Li$_3$Cr tetrahedron and compared the energy of Cr in the octahedral site and Cr in the tetrahedral site of the Li$_3$Cr tetrahedron. To understand how local environment influences the Cr site energy difference, we also removed additional Li ions in the first neighbouring coordination shell (Supplementary Fig. 16) of Cr to create quad-vacancy, penta-vacancy and hex-vacancy configurations. All density functional theory calculations used the SCAN functional, as described in the Methods. The results, shown in Fig. 5b, indicate that the driving force for Cr moving to a tetrahedral site is generally higher in PD-LCMO than in the layered structure. This is consistent with the EXAFS results (Fig. 5a), which indicate that Cr$_{tet}$ forms earlier during charge in PD-LCMO compared with L-LCMO.

Once Cr migrates to the tetrahedral site in the Li slab of the layered structure, the Li ion immediately below the Cr vacancy can migrate to its face-sharing tetrahedral site (bottom tetrahedral site in Fig. 5c)
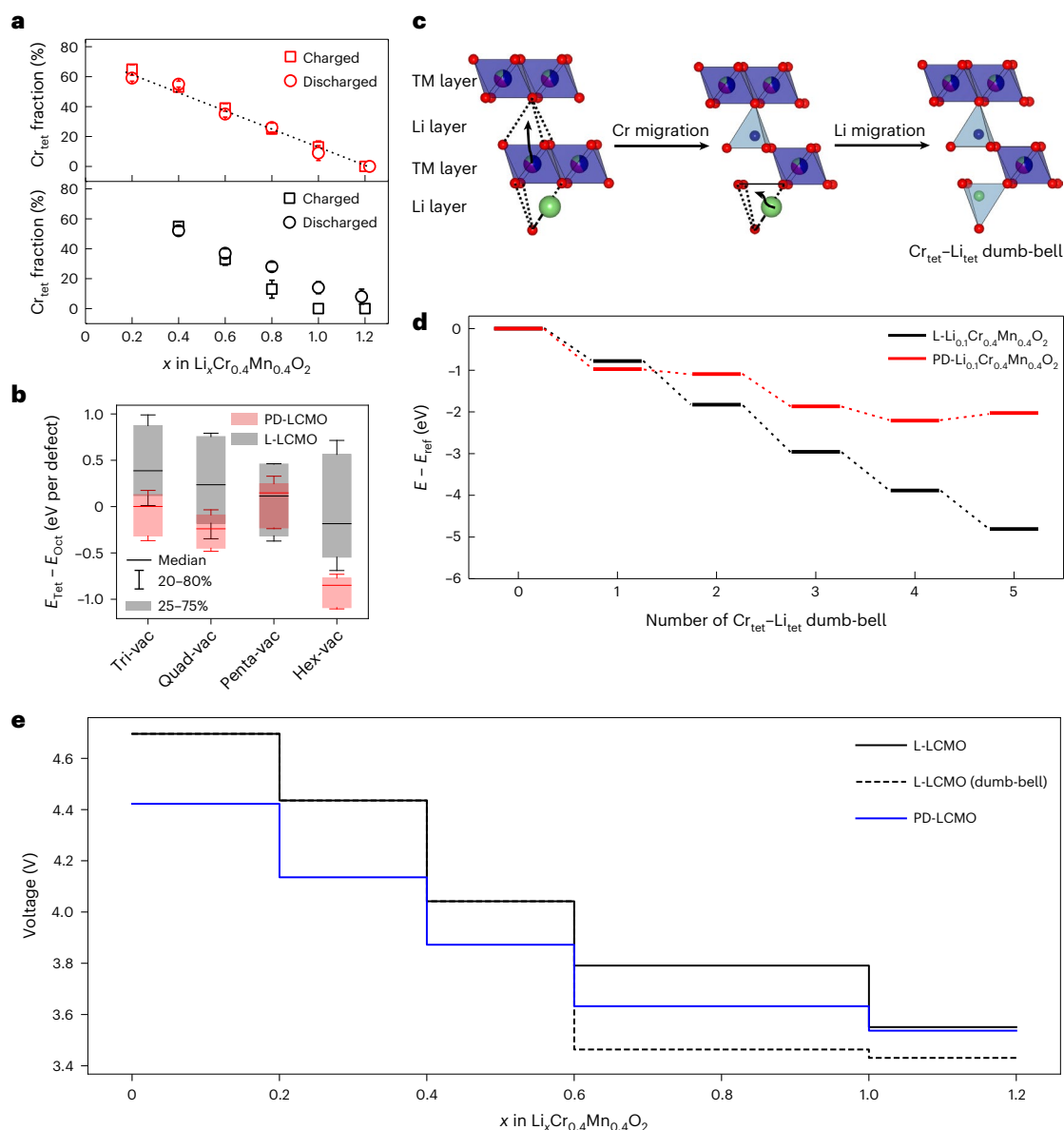
Fig. 5 | Cr migration and tetrahedral dumb-bell formation in layered and disordered structures. a, Cr_{tet} content determined from EXAFS fitting in L-LCMO (bottom) and PD-LCMO (top). The error bars indicate the standard deviation of the fitted Cr_{tet} content. The dashed line shows that the relationship between Cr_{tet} fraction and Li content follows a linear trend. **b**, Calculated formation energies of Cr_{tet} in the L-LCMO and PD-LCMO. Cr oct–tet migration was considered to occur in Li_3Cr tetrahedra. All three Li atoms in the Li_3M tetrahedron were removed (Li tri-vacancy) to allow Cr migration. The surrounding Li atoms that are not in the Li_3M tetrahedron were removed in a stepwise manner to capture the evolution of the site energy difference at other Li vacancy (vac) concentrations (quad-vac, penta-vac and hex-vac). For each Li vacancy

concentration, there are 50 and 22 data points for PD-LCMO and L-LCMO, respectively. **c**, Illustration of Cr_{tet}–Li_{tet} dumb-bell formation. Li, Cr, Mn and O are shown in green, blue, purple and red, respectively. **d**, Energy change when forming a certain number of Cr_{tet}–Li_{tet} dumb-bells in L- and PD- $Li_{0.1}Cr_{0.4}Mn_{0.4}O_2$ supercells of 100 cations. The state with all cations occupying octahedral sites is used as energy reference (E_{ref}), and the relative energy was calculated as $E - E_{ref}$ in the presence of 1, 2, 3, 4 or 5 Cr_{tet}–Li_{tet} dumb-bells. The dashed lines connect the calculated energies to show the energy change from 0 to 5 Cr_{tet}–Li_{tet} dumb-bells. **e**, Calculated voltage curves of three different lithiation mechanisms, lithiation in L-LCMO without dumb-bell complexes, lithiation in L-LCMO with dumb-bell complexes and lithiation in PD-LCMO.

forming a Cr_{tet}–Li_{tet} dumb-bell. Such dumb-bells have been shown to lower the energy in Mn-based systems and have in general been shown to assist TM migration into a tetrahedral site[29–31]. As shown in Fig. 5c, the geometry of the layered structure will always orient the dumb-bells perpendicular to the TM/Li layer. However, the orientation of the dumb-bells in a disordered structure will be random due to the absence of any specific TM/Li layering. In Fig. 5d,e we show the results from ab initio calculations that support the relation between hysteresis and dumb-bell formation. Figure 5d shows the change in energy as more dumb-bells are introduced in L- or PD- $Li_{0.1}Cr_{0.4}Mn_{0.4}O_2$. Not only does

the formation of Cr_{tet}–Li_{tet} dumb-bells lower the energy in L-LCMO more than in PD-LCMO, the energy continues to decrease in L-LCMO with more dumb-bells, whereas PD-LCMO achieves an energy minimum at a certain concentration of dumb-bells. This higher stability and favourable interaction of dumb-bells in L-LCMO will lead to more collective, and therefore more hysteretic, dumb-bell creation than in PD-LCMO. The preference for forming dumb-bell complexes in L-LCMO is related to its layered structure, which forces dumb-bells to orient parallel to each other[29,30]. As indicated in previous studies[29,30], such alignment in L-LCMO creates an attractive interaction between Li–TM dumb-bells,
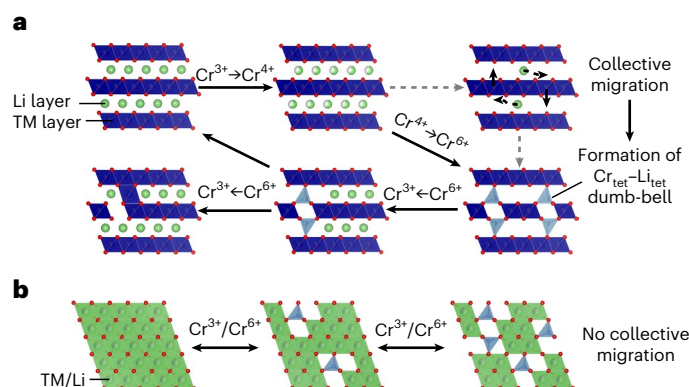
Fig. 6 | Proposed reaction mechanisms in L-LCMO and PD-LCMO. a, Schematic showing Cr redox and migration in L-LCMO. Cr^{3+} is initially oxidized to Cr^{4+} and then to Cr^{6+} upon charging. At the top of charge collective migration of Cr to the tetrahedral site in the Li layers occurs, and Cr_{tet} induces the formation of Cr_{tet}–Li_{tet} dumb-bells that stabilize the layered structure. The dashed grey arrows show a possible intermediate step to form the Cr_{tet}–Li_{tet} dumb-bells at the top of charge. The lowered energy is lost in the form of heat, causing voltage hysteresis. In the discharge process, Cr^{6+} is gradually reduced to Cr^{3+} showing irreversible Cr migration upon charging and discharging. **b**, Schematic showing reversible Cr^{3+}/Cr^{6+} redox and Cr migration in PD-LCMO.

making them appear and disappear in a more collective manner than the isolated dumb-bell formation that would occur in PD-LCMO.

To provide direct evidence of how the dumb-bell complex is related to the shape of the voltage curve, we performed density functional theory calculations on the voltage profiles of PD-LCMO, L-LCMO and L-LCMO with dumb-bell complexes at the end of discharge in Fig. 5e. The pseudo-binary convex hulls of $Cr_{0.4}Mn_{0.4}O_2$–$Li_{1.2}Cr_{0.4}Mn_{0.4}O_2$ of all three groups of calculations are shown in Supplementary Fig. 17. For the calculations for PD-LCMO and L-LCMO, direct structural enumeration was performed to sample 25 structures at each discharge state. In the calculations for L-LCMO with dumb-bell structures, the structures were sampled by randomly placing Cr_{tet}–Li_{tet} dumb-bells into lattices with given Li contents. At each discharge state, all possible Cr_{tet}–Li_{tet} dumb-bell configurations were enumerated while random sampling was performed to generate a specific Li–Cr dumb-bell concentration. The amount of Cr_{tet}–Li_{tet} dumb-bells was determined by the average charge states of Cr (that is, equal to the amount of Cr^{6+} assuming all oxidized Cr is Cr^{6+}). At the end of discharge (that is, 1.2 Li per formula unit), two Cr_{tet}–Li_{tet} dumb-bells per structure were still generated to simulate the experimentally observed Cr_{tet} in L-LCMO (Fig. 5a). Dumb-bell complexes were only generated for Li contents >0.6 as this is close to the composition where a significant voltage drop starts to occur in the experimental voltage profile (Fig. 2b). The calculated voltage curves of PD-LCMO and L-LCMO without dumb-bells have similar shapes. However, L-LCMO with dumb-bell structures showed a significant voltage drop at the end of discharge clearly showing that the dumb-bell complexes cause a voltage drop. These results strongly suggest that the significant voltage hysteresis in L-LCMO is correlated with the stabilization of the Cr_{tet}–Li_{tet} dumb-bell complexes in the ordered structure.

Multi-electron redox from a TM ion is highly desirable to increase the reversible capacity in battery cathodes. In this study, we compared the reversibility of the Cr^{3+}/Cr^{6+} three-electron redox in L-LCMO and PD-LCMO. While both L-LCMO and PD-LCMO derived a capacity >300 mAh g^{-1} from Cr redox, PD-LCMO showed a much smaller voltage hysteresis and a 47% larger discharge energy density (1,132 Wh kg^{-1}) than L-LCMO when cycled between 4.8 and 1.5 V. To verify that the superior performance of PD-LCMO does not result from a difference in particle size, we ball milled L-LCMO at 300 r.p.m. for 1 h to reduce its particle size. While we found that particle size reduction

increased the charge and discharge capacities, the prominent voltage hysteresis remained present in L-LCMO (Supplementary Note 3 and Supplementary Fig. 18). We also prepared a fully disordered LCMO and found significantly reduced voltage hysteresis and superior rate capability similar to PD-LCMO (Supplementary Fig. 19), confirming that the different electrochemistry between L-LCMO and PD-LCMO mainly originates from their different structures (layered versus disordered).

Figure 6 shows our hypothesis for the different reaction pathways of L-LCMO and PD-LCMO. As demonstrated by the X-ray absorption spectroscopy (XAS) results, in L-LCMO the redox pathway (Cr^{6+}→Cr^{3+}) in lithiation does not retrace the delithiation oxidation sequence (Cr^{3+}→Cr^{4+}→Cr^{6+}). Upon delithiation of $Li_xCr_{0.4}Mn_{0.4}O_2$ ($x \geq 0.8$), Cr^{4+} forms and remains in an octahedral site as d^2 Cr^{4+} is not particularly mobile. In contrast, the fully oxidized Cr^{6+} at the top of charge easily migrates to the tetrahedral site as its d^0 configuration provides no ligand field stabilization in the octahedral site. Upon lithiation Cr^{6+} is reduced to Cr^{3+}, yet some Cr^{6+} remains for $x > 0.8$ in $Li_xCr_{0.4}Mn_{0.4}O_2$, leading to hysteretic Cr migration.

In contrast, the XAS on PD-LCMO indicated reversible Cr^{3+}/Cr^{6+} three-electron redox and non-hysteretic Cr migration upon charge and discharge. The preferential and reversible formation of tetrahedral Cr^{6+} early in the charge process in PD-LCMO is facilitated by the good match between the tetrahedron height and the size of Cr^{6+}. If the tetrahedron height is too large for the short metal–oxygen bonds, the tetrahedral TM is destabilized. An example of this is the large tetrahedron height in layered $NaCrO_2$ that inhibits Cr migration up to a desodiated state of $Na_{0.4}CrO_2$ (ref. 32). Based on the refined c lattice parameter, the average tetrahedron height in pristine L-LCMO and PD-LCMO is 2.39 Å, yet the actual tetrahedron height in the Li layer of L-LCMO should be larger than 2.39 Å because the Li slab distance in pristine L-LCMO is 2.63 Å. Upon delithiation to $Li_{0.8}Cr_{0.4}Mn_{0.4}O_2$, the average tetrahedron height in L-LCMO increases to 2.41 Å, and the slab distance increases to 2.65 Å. These dimensional changes increase the energy for Cr_{tet} in the Li layer, tipping the balance towards oxidation of Cr to Cr^{4+}_{oct} as the first oxidation process in L-LCMO. In contrast, the presence of disorder makes the tetrahedral coordination environment in PD-LCMO more isotropic, and significant lattice expansion is not observed upon delithiation (Fig. 3b and Supplementary Fig. 8), both of which lower the energy for Cr in the tetrahedral site at $Li_xCr_{0.4}Mn_{0.4}O_2$ ($x \geq 0.8$), making it a more favourable oxidation path than Cr^{4+}_{oct}. Thus, L-LCMO and PD-LCMO show different Cr migration behaviour during the charge process. Although this does not necessarily imply a difference in hysteresis between L-LCMO and PD-LCMO, our computational analysis showed a fundamental difference in the Cr migration energetics in L-LCMO and PD-LCMO: compared with PD-LCMO, the energy decrease in L-LCMO is larger when Cr_{tet}–Li_{tet} dumb-bells form, and continues to decrease as more dumb-bells form, indicating an attractive interaction between them. This reinforcing interaction by which more dumb-bells lead to increased stabilization is caused by the coupling through the slab spacing: as Cr^{6+} migrates it further reduces the slab spacing and the size of the tetrahedral site in the Li layer, making it more favourable for Cr^{6+}. It is this coupling between slab spacing and Cr^{6+} migration that creates the collective effect. Upon discharge, the stabilized Cr_{tet} inhibits the expansion of the c lattice parameter and its migration back to the octahedral site in the TM layer, causing hysteresis in the voltage, as confirmed by the computed voltage curves. Owing to the lack of well-defined order in disordered materials the dumb-bells are more randomly oriented, limiting the collective effect in PD-LCMO and making the voltage non-hysteretic.

The Cr-based material is an ideal system to investigate the impact of TM migration on voltage hysteresis because the fully oxidized Cr^{6+} is highly mobile. The introduction of Cr^{3+}/Cr^{6+} redox in layered NMC materials generally leads to low energy efficiency/large voltage hysteresis[33,34], while the Cr^{3+}/Cr^{6+} three-electron redox is reversibly utilized in a more disordered structures[35–37]. Other redox systems with mobile cations (that is, Mo^{3+}/Mo^{6+} and V^{3+}/V^{5+}) also show high electrochemical

performance in disordered structures[22,23,35,38–40], further corroborating that (partially) disordered structures can accommodate a high degree of TM migration by reducing their ability to make the motion collectively. To test the generalizability of the voltage hysteresis mitigation strategy, we also compared layered and partially disordered $Li_{1.05}V_{0.85}Ti_{0.1}O_2$ (L-LVTO and PD-LVTO) (Supplementary Note 4, Supplementary Fig. 20 and Supplementary Table 5). L-LVTO showed a large charge capacity of 240 mAh g^{-1} but delivered a limited discharge capacity of 104 mAh g^{-1} between 4.3 and 1.3 V. In contrast, PD-LVTO delivered a reversible capacity of ~275 mAh g^{-1}, which probably benefits from reduced voltage hysteresis as observed in LCMO (Fig. 2c). The inhibition of the collective TM migration in disordered structures may foster a rethinking of other collective effects that limit the performance in ordered electrode materials. For example, while the Jahn–Teller active Mn^{3+} is not desirable for cathode design as a collective Jahn–Teller distortion causes large anisotropic lattice change limiting structural reversibility[41,42], a random cation arrangement may reduce such collective distortion effect.

In conclusion, we have shown that cation disorder inhibits collective Cr migration in LCMO and reduces the internal energy dissipation and voltage hysteresis associated with Cr migration. Owing to the more reversible Cr migration in the disordered structure, PD-LCMO showed significantly improved electrochemistry with high energy density and good cycling stability relative to L-LCMO. We believe that the inhibition of the collective effects upon cation disordering provides a new opportunity to design high-performance cathode materials.

Online content

Any methods, additional references, Nature Portfolio reporting summaries, source data, extended data, supplementary information, acknowledgements, peer review information; details of author contributions and competing interests; and statements of data and code availability are available at https://doi.org/10.1038/s41563-022-01467-z.

References

1. Goodenough, J. B. & Park, K.-S. The Li-ion rechargeable battery: a perspective. *J. Am. Chem. Soc.* **135**, 1167–1176 (2013).
2. Manthiram, A. An outlook on lithium ion battery technology. *ACS Cent. Sci.* **3**, 1063–1069 (2017).
3. Seo, D.-H. et al. The structural and chemical origin of the oxygen redox activity in layered and cation-disordered Li-excess cathode materials. *Nat. Chem.* **8**, 692–697 (2016).
4. Nayak, P. K. et al. Review on challenges and recent advances in the electrochemical performance of high capacity Li- and Mn-rich cathode materials for Li-ion batteries. *Adv. Energy Mater.* **8**, 1702397 (2018).
5. Gent, W. E. et al. Coupling between oxygen redox and cation migration explains unusual electrochemistry in lithium-rich layered oxides. *Nat. Commun.* **8**, 2091 (2017).
6. House, R. A. et al. First-cycle voltage hysteresis in Li-rich 3*d* cathodes associated with molecular O_2 trapped in the bulk. *Nat. Energy* **5**, 777–785 (2020).
7. Balasubramanian, M., McBreen, J., Davidson, I. J., Whitfield, P. S. & Kargina, I. In situ X-ray absorption study of a layered manganese-chromium oxide-based cathode material. *J. Electrochem. Soc.* **149**, A176–A184 (2002).
8. Lyu, Y. et al. Probing reversible multielectron transfer and structure evolution of $Li_{1.2}Cr_{0.4}Mn_{0.4}O_2$ cathode material for Li-ion batteries in a voltage range of 1.0–4.8 V. *Chem. Mater.* **27**, 5238–5252 (2015).
9. Ammundsen, B. et al. Local structure and first cycle redox mechanism of layered $Li_{1.2}Cr_{0.4}Mn_{0.4}O_2$ cathode material. *J. Electrochem. Soc.* **149**, A431–A436 (2002).
10. Lu, Z. & Dahn, J. R. In situ and ex situ XRD investigation of $Li[Cr_xLi_{1/3-x/3}Mn_{2/3-2x/3}]O_2$ (x=1/3) cathode material. *J. Electrochem. Soc.* **150**, A1044–A1051 (2003).
11. Lu, Z. & Dahn, J. R. Structure and electrochemistry of layered $Li[Cr_xLi_{(1/3-x/3)}Mn_{(2/3-2x/3)}]O_2$. *J. Electrochem. Soc.* **149**, A1454 (2002).
12. Zhang, L. & Noguchi, H. Novel layered Li Cr Ti O cathode materials related to the $LiCrO_2$ Li_2TiO_3 solid solution. *J. Electrochem. Soc.* **150**, A601–A607 (2003).
13. Mi, X., Li, H. & Huang, X. Carbon-coated $Li_{1.2}Cr_{0.4}Ti_{0.4}O_2$ cathode material for lithium-ion batteries. *Electrochem. Solid State Lett.* **9**, A324–A327 (2006).
14. Zhang, L. & Noguchi, H. Novel layered Li–Cr–Ti–O cathode materials for lithium rechargeable batteries. *Electrochem. Commun.* **4**, 560–564 (2002).
15. Mi, X., Li, H. & Huang, X. Electrochemical and structural studies of the carbon-coated $Li[Cr_xLi_{(1/3-x/3)}Ti_{(2/3-2x/3)}]O_2$ (x=0.3, 0.35, 0.4, 0.45). *J. Power Sources* **174**, 867–871 (2007).
16. Eum, D. et al. Voltage decay and redox asymmetry mitigation by reversible cation migration in lithium-rich layered oxide electrodes. *Nat. Mater.* **19**, 419–427 (2020).
17. Boldyrev, V. V. Mechanochemistry and mechanical activation of solids. *Russ. Chem. Rev.* **75**, 177–189 (2006).
18. Shi, T. et al. Shear-assisted formation of cation-disordered rocksalt $NaMO_2$ (M = Fe or Mn). *Chem. Mater.* **30**, 8811–8821 (2018).
19. House, R. A. et al. Lithium manganese oxyfluoride as a new cathode material exhibiting oxygen redox. *Energy Environ. Sci.* **11**, 926–932 (2018).
20. Luo, K. et al. Charge-compensation in 3*d*-transition-metal-oxide intercalation cathodes through the generation of localized electron holes on oxygen. *Nat. Chem.* **8**, 684–691 (2016).
21. Lee, J. et al. Reversible Mn^{2+}/Mn^{4+} double redox in lithium-excess cathode materials. *Nature* **556**, 185–190 (2018).
22. Takeda, N. et al. Reversible Li storage for nanosize cation/anion-disordered rocksalt-type oxyfluorides: $LiMoO_2$–x LiF (0 ≤ x ≤ 2) binary system. *J. Power Sources* **367**, 122–129 (2017).
23. Takeda, N., Ikeuchi, I., Natsui, R., Nakura, K. & Yabuuchi, N. Improved electrode performance of lithium-excess molybdenum oxyfluoride: titanium substitution with concentrated electrolyte. *ACS Appl. Energy Mater.* **2**, 1629–1633 (2019).
24. Suo, L. et al. Fluorine-donating electrolytes enable highly reversible 5-V-class Li metal batteries. *Proc. Natl Acad. Sci. USA* **115**, 1156 LP–1151161 (2018).
25. Wang, J. et al. Superconcentrated electrolytes for a high-voltage lithium-ion battery. *Nat. Commun.* **7**, 12032 (2016).
26. Davenport, A. J. et al. In situ X-ray absorption study of chromium valency changes in passive oxides on sputtered AlCr thin films under electrochemical control. *J. Electrochem. Soc.* **138**, 337–338 (1991).
27. Manceau, A. & Charlet, L. X-ray absorption spectroscopic study of the sorption of Cr(III) at the oxide-water interface: I. Molecular mechanism of Cr(III) oxidation on Mn oxides. *J. Colloid Interface Sci.* **148**, 425–442 (1992).
28. Reed, J. & Ceder, G. Role of electronic structure in the susceptibility of metastable transition-metal oxide structures to transformation. *Chem. Rev.* **104**, 4513–4534 (2004).
29. Reed, J., Ceder, G. & Van Der Ven, A. Layered-to-spinel phase transition in Li_xMnO_2. *Electrochem. Solid State Lett.* **4**, A78 (2001).
30. Bréger, J. et al. Effect of high voltage on the structure and electrochemistry of $LiNi_{0.5}Mn_{0.5}O_2$: a joint experimental and theoretical study. *Chem. Mater.* **18**, 4768–4781 (2006).
31. Kim, S., Ma, X., Ong, S. P. & Ceder, G. A comparison of destabilization mechanisms of the layered Na_xMO_2 and Li_xMO_2 compounds upon alkali de-intercalation. *Phys. Chem. Chem. Phys.* **14**, 15571–15578 (2012).
32. Bo, S.-H., Li, X., Toumar, A. J. & Ceder, G. Layered-to-rock-salt transformation in desodiated Na_xCrO_2 (x 0.4). *Chem. Mater.* **28**, 1419–1429 (2016).

33. Lee, E. et al. Role of Cr^{3+}/Cr^{6+} redox in chromium-substituted $Li_2MnO_3 \cdot LiNi_{1/2}Mn_{1/2}O_2$ layered composite cathodes: electrochemistry and voltage fade. *J. Mater. Chem. A* **3**, 9915–9924 (2015).

34. Karan, N. K. et al. Morphology, structure, and electrochemistry of solution-derived $LiMn_{0.5-x}Cr_{2x}Ni_{0.5-x}O_2$ for lithium-ion cells. *J. Electrochem. Soc.* **156**, A553–A562 (2009).

35. Ren, S. et al. Improved voltage and cycling for Li^+ intercalation in high-capacity disordered oxyfluoride cathodes. *Adv. Sci.* **2**, 1500128 (2015).

36. Huang, J. et al. Non-topotactic reactions enable high rate capability in Li-rich cathode materials. *Nat. Energy* **6**, 706–714 (2021).

37. Zheng, X. et al. Reversible Mn/Cr dual redox in cation-disordered Li-excess cathode materials for stable lithium ion batteries. *Acta Mater.* **212**, 116935 (2021).

38. Hoshino, S. et al. Reversible three-electron redox reaction of Mo^{3+}/Mo^{6+} for rechargeable lithium batteries. *ACS Energy Lett.* **2**, 733–738 (2017).

39. Nakajima, M. & Yabuuchi, N. Lithium-excess cation-disordered rocksalt-type oxide with nanoscale phase segregation: $Li_{1.25}Nb_{0.25}V_{0.5}O_2$. *Chem. Mater.* **29**, 6927–6935 (2017).

40. Chen, R. et al. Disordered lithium-rich oxyfluoride as a stable host for enhanced Li^+ intercalation storage. *Adv. Energy Mater.* **5**, 1401814 (2015).

41. Yamada, A., Tanaka, M., Tanaka, K. & Sekai, K. Jahn–Teller instability in spinel Li–Mn–O. *J. Power Sources* **81–82**, 73–78 (1999).

42. Zuo, C. et al. Double the capacity of manganese spinel for lithium-ion storage by suppression of cooperative Jahn–Teller distortion. *Adv. Energy Mater.* **10**, 2000363 (2020).

Methods

Synthesis

L-LCMO was synthesized using a solid-state method. Li_2CO_3, Cr_2O_3 and MnO_2 were used as precursors, and 5% excess Li_2CO_3 was used to compensate for Li loss during synthesis. The ball-milled mixture was pelletized and then heated at 950 °C for 10 h under an Ar atmosphere. PD-LCMO was prepared by ball milling (SPEX 8000 M Mix) the L-LCMO. L-LCMO powder (0.5 g) was added to an Ar-filled 45 ml zirconia jar, and 10 g of yttria-stabilized zirconia balls (5 mm) were used as the grinding media. To obtain PD-LCMO, the L-LCMO was ball milled for 1 h using a SPEX 8000 M Mixer. D-LCMO was prepared by ball milling for a longer period (20 h): 1.0 g of L-LCMO was added to an Ar-filled 50 ml stainless steel grinding jar, and stainless steel balls (5 10-mm-diameter balls and and 10 5-mm-diameter balls) were used as grinding media. To obtain D-LCMO, the L-LCMO was ball milled for 20 h using a Retsch PM 200 at 450 r.p.m.

L-LVTO was synthesized using a solid-state method. Li_2CO_3, V_2O_3 and TiO_2 were used as precursors, and 5% excess Li_2CO_3 was used to compensate for Li loss during synthesis. The ball-milled mixture was pelletized and then heated at 800 °C for 5 h under a 2% H_2/Ar atmosphere. PD-LVTO was prepared using the 1 h ball-milling procedure described above.

Electrochemistry

The active material, carbon black (Timcal, SUPER C65) and polytetrafluoroethylene (PTFE, DuPont, Teflon 8A) were mixed in a weight ratio of 70:20:10. The mixture was then rolled into a thin film inside an argon-filled glove box. 1 M $LiPF_6$ in 1:1 (volume ratio) ethylene carbonate and DMC (BASF) was used as the electrolyte. The concentrated electrolyte, LiFSI:DMC in a molar ratio of 1:1.1, was prepared by dissolving the LiFSI salt into the DMC solution in an Ar-filled glove box. Coin cells were assembled using the cathode film, Li metal foil, electrolyte and separators (Whatman glass microfibre filter) in an Ar-filled glove box. The loading density of the active material was approximately 3 mg cm^{-2} for each cathode film. Galvanostatic cycling tests were performed at room temperature using an Arbin battery tester. Galvanostatic intermittent titration technique measurements were performed by charging/discharging the cell for 10 min at a current density of 50 mA g^{-1} and relaxing for 5 h to reach a quasi-equilibrium state. Electrochemically delithiated/lithiated samples were prepared by charging/discharging the cells at a current density of 20 mA g^{-1}, and the charged/discharged cathode films were collected after washing with DMC in an Ar-filled glove box. Cathode films consisting of 70% PD-LCMO, 20% carbon black and 10% polyvinylidene fluoride were used for synchrotron-based ex situ XRD measurements.

Characterization

XRD patterns of the as-prepared LCMO materials were collected at 11-BM at the Advanced Photon Source, Argonne National Laboratory. Time-of-flight neutron diffraction experiments were performed at the Spallation Neutron Source at Oak Ridge National Laboratory on the Nanoscale Ordered Materials Diffractometer. Rietveld refinement of XRD and neutron diffraction was performed using the TOPAS software (version 6, Bruker AXS). XRD patterns of the as-prepared LVTO materials were collected at the Stanford Synchrotron Radiation Lightsource. To compare the XRD data collected from different sources, the XRD patterns were converted to patterns based on Cu K-alpha (1.54 Å).

Scanning electron microscopy images were captured using a Zeiss Gemini Ultra-55 analytical field-emission scanning electron microscope under acceleration voltages of 5–10 kV. High-resolution STEM images were obtained using the TEAM I microscope (a modified FEI Titan 80–300 microscope with double-aberration-corrected scanning transmission electron microscope) at the Molecular Foundry at Lawrence Berkeley National Laboratory using an acceleration voltage of 300 kV. The TEM characterization was performed using a JEM-2100F at 200 kV.

Hard X-ray absorption spectroscopy

Cr K-edge and Mn K-edge XAS was performed at beamline 20BM at the Advanced Photon Source, Argonne National Laboratory. The measurements were performed in transmission mode using a Si(111) monochromator. A Cr foil (5989 eV) or Mn foil (6539 eV) was simultaneously measured with the experimental measurements to calibrate the energy of the individual datasets. All the ex situ samples were sealed between polyimide tape to avoid exposure to air. The XAS spectra were calibrated and normalized using the Athena software packages[43,44]. The background contribution was limited below radial distance (R_{bkg}) = 1.0 using the built-in AUTOBK algorithm. The normalized spectra were converted from energy to wave-vector **k** and then Fourier transformed from **k** space to **R** space. Because the Fourier transform was not phase corrected, the **R** values should be ~0.3 to 0.4 shorter than the actual distances[7]. The EXAFS spectra of the Cr edge were analysed using the Artemis software packages (version 0.9.26) refs. [43,44]. The EXAFS fitting was conducted using a Hanning window in k, k^2 and k^3 k-weights simultaneously. The first (Cr–O) and second (Cr–Cr/Mn) shells were fitted over the R range of 1–3 Å. The structural models for the fittings were adapted from structures calculated with density functional theory (DFT). The Cr–O and Cr–Cr/Mn single scattering paths were used to fit the octahedral Cr–O and Cr–Cr/Mn bonds, respectively. To fit the EXAFS spectra with the tetrahedral Cr–O contribution, a Cr–O path (1.65 Å) generated by FEFF calculation was added to the structural models. The amplitude reduction factor S_0^2 was determined by fitting the Cr foil EXAFS spectrum, and the obtained value (0.7) was used for all the fits. The k^2-weighted EXAFS spectra are shown in the figures.

Computational methods

First-principles DFT calculations in combination with cluster expansion Monte Carlo simulations were performed to determine the atomic configurations and Cr defect energetics. To efficiently sample the atomic ordering within the $LiCrO_2$–Li_2MnO_3 composition space, a cluster expansion consisting of pair interactions up to 7.1 Å, triplet interactions up to 4.0 Å and quadruplet interactions up to 4.0 Å based on a primitive rocksalt lattice was constructed using energies calculated via DFT. All interactions were taken relative to a baseline electrostatic energy defined with respect to the formal charges of the ionic species with a fitted dielectric constant. The effective cluster interactions and dielectric constant were determined from a L1-regularized least-squares regression with the regularization parameters selected to minimize cross-validation errors[45]. Using this procedure, a root-mean-squared error below 7.5 meV per atom was obtained by fitting 960 DFT-calculated structures.

All of the DFT calculations used to fit the cluster expansion were performed using the projector-augmented wave method[46], as implemented in the Vienna ab initio Simulation Package (version 6.2.0)[47]. A rotationally averaged Hubbard U correction[48] was used to correct the self-interaction error for Cr and Mn. The U parameters were obtained from a previously reported calibration to oxide formation energies[49]. Calculations for Cr migration and dumb-bell formation were performed with the SCAN meta-GGA exchange-correlation functional because of its better performance in capturing the relative energy difference of delithiated states[21,50–52]. For both the GGA+U and SCAN calculations, a reciprocal space discretization of 25 K-points per Å^{-1} was applied, and the convergence criteria were set to 10^{-6} eV for electronic loops and 0.02 eV Å^{-1} for ionic loops. After fitting the cluster expansion model, Monte Carlo sampling was applied to obtain representative structures at experimental synthesis conditions for further evaluation of the Cr defect energetics. For L-LCMO, Monte Carlo simulations were performed at 1,273 K with the constraint that both Cr^{3+} and Mn^{4+} can only remain in the TM layer. For PD-LCMO, full Monte Carlo simulations were performed, allowing Cr^{3+} and Mn^{4+} to be swapped to all the octahedral cation sites. Given that PD-LCMO was synthesized under high-energy ball-milling

conditions, an equivalent temperature of 2,573 K was applied to create cation disorder[52–54]. It is worth noting that even at 2,573 K, the structure generated was still not fully disordered compared with our simulations on other cation-disordered rocksalt materials due to the significant resistance of Cr^{3+} has to disordering[53–55]. The structures we generated can therefore be regarded as close to the PD-LCMO structures we obtained in experiments. For both L-LCMO and PD-LCMO, three Monte Carlo structures were generated with a supercell size of $3 \times 4 \times 5$.

In the Monte Carlo structures, all the Cr atoms remaining adjacent to three Li atoms form Li_3M (M = Cr) tetrahedra. Each of these Cr atoms can potentially migrate from the corner to the centre of the Li_3M tetrahedron (Supplementary Fig. 11) upon delithiation. Therefore, by evaluating the energy difference before and after Cr migration into a Li_3M site for all the Cr atoms, we could obtain good statistics on the Cr site energetics in different local environments. It is known that all three Li atoms in the Li_3M tetrahedron should be removed (Li tri-vacancy) to trigger Cr migration, as there would otherwise be large electrostatic repulsion between Cr with remaining Li[56,57]. Starting from the tri-vacancy case, other surrounding Li atoms that were not in the Li_3M tetrahedron but within the first-neighbour-cation coordination shell were removed stepwise to capture the evolution of the site energy difference as a function of local composition. As a result, four different local Li vacancy concentrations were considered, that is, tri-vacancy, quad-vacancy, penta-vacancy and hex-vacancy. At each local vacancy concentration, DFT calculations with SCAN functionals were performed to obtain accurate energetics of Cr at either the octahedral site (E_{Oct}) or Li_3M tetrahedral site (E_{Tet}). The energy difference between the two configurations ($E_{Tet} - E_{Oct}$) was used to quantify the tendency of Cr migration as a negative value indicates that it is energetically favourable for Cr to migrate to the Li_3M tetrahedron site.

To calculate the energy change in the presence of Cr_{tet}–Li_{tet} dumb-bells in the L-LCMO and PD-LCMO, the delithiated state ($Li_{0.1}Cr_{0.4}Mn_{0.4}O_2$) with all cations occupying octahedral sites was used as energy reference (E_{oct}), and the relative energies of forming Cr_{tet}–Li_{tet} dumb-bells were calculated as $E - E_{oct}$. For both layered and disordered structures, the energy differences were averaged among 10 sampled structures from cluster expansion Monte Carlo simulations. For each of the structures, Li and Cr positions were rearranged accordingly to reach 1, 2, 3, 4 and 5 Cr_{tet}–Li_{tet} dumb-bells, respectively. For all three groups of voltage curve calculations in Fig. 5, 25 structures were generated at each Li content (that is, 0, 0.2, 0.4, 0.6, 0.8, 1.0 and 1.2 per functional unit). All of the calculations on dumb-bell complexes and voltage curves were also done with SCAN functionals on the Monte Carlo structures generated with $3 \times 4 \times 5$ supercells as described above.

Data availability
All data generated and analysed during this study are included in the published article and its Supplementary Information. Source data are provided with this paper.

References

43. Ravel, B. & Newville, M. ATHENA, ARTEMIS, HEPHAESTUS: data analysis for X-ray absorption spectroscopy using IFEFFIT. *J. Synchrotron Radiat.* **12**, 537–541 (2005).
44. Ravel, B. & Newville, M. ATHENA and ARTEMIS interactive graphical data analysis using IFEFFIT. *Phys. Scr.* **2005**, 1007 (2005).
45. Nelson, L. J., Hart, G. L. W., Zhou, F. & Ozoliņš, V. Compressive sensing as a paradigm for building physics models. *Phys. Rev. B* **87**, 35125 (2013).
46. Kresse, G. & Joubert, D. From ultrasoft pseudopotentials to the projector augmented-wave method. *Phys. Rev. B* **59**, 1758–1775 (1999).
47. Kresse, G. & Furthmüller, J. Efficiency of ab-initio total energy calculations for metals and semiconductors using a plane-wave basis set. *Comput. Mater. Sci.* **6**, 15–50 (1996).
48. Dudarev, S. L., Botton, G. A., Savrasov, S. Y., Humphreys, C. J. & Sutton, A. P. Electron-energy-loss spectra and the structural stability of nickel oxide: An LSDA+U study. *Phys. Rev. B* **57**, 1505–1509 (1998).
49. Wang, L., Maxisch, T. & Ceder, G. Oxidation energies of transition metal oxides within the GGA+U framework. *Phys. Rev. B* **73**, 195107 (2006).
50. Sun, J., Ruzsinszky, A. & Perdew, J. P. Strongly constrained and appropriately normed semilocal density functional. *Phys. Rev. Lett.* **115**, 36402 (2015).
51. Kitchaev, D. A. et al. Energetics of MnO_2 polymorphs in density functional theory. *Phys. Rev. B* **93**, 45132 (2016).
52. Kitchaev, D. A. et al. Design principles for high transition metal capacity in disordered rocksalt Li-ion cathodes. *Energy Environ. Sci.* **11**, 2159–2171 (2018).
53. Lun, Z. et al. Design principles for high-capacity Mn-based cation-disordered rocksalt cathodes. *Chem* **6**, 153–168 (2020).
54. Richards, W. D., Dacek, S. T., Kitchaev, D. A. & Ceder, G. Fluorination of lithium-excess transition metal oxide cathode materials. *Adv. Energy Mater.* **8**, 1701533 (2018).
55. Ouyang, B. et al. Effect of fluorination on lithium transport and short-range order in disordered-rocksalt-type lithium-ion battery cathodes. *Adv. Energy Mater.* **10**, 1903240 (2020).
56. Vinckevičiūtė, J., Radin, M. D., Faenza, N. V., Amatucci, G. G. & Van der Ven, A. Fundamental insights about interlayer cation migration in Li-ion electrodes at high states of charge. *J. Mater. Chem. A* **7**, 11996–12007 (2019).
57. Radin, M. D., Vinckeviciute, J., Seshadri, R. & Van der Ven, A. Manganese oxidation as the origin of the anomalous capacity of Mn-containing Li-excess cathode materials. *Nat. Energy* **4**, 639–646 (2019).

Acknowledgements

Author contributions

J.H. and G.C. planned the project. G.C. supervised all aspects of the research. J.H. synthesized, characterized and

Competing interests

The authors declare no competing interests.

Additional information

Supplementary information The online version contains supplementary material available at https://doi.org/10.1038/s41563-022-01467-z.

Correspondence and requests for materials should be addressed to Gerbrand Ceder.

Peer review information *Nature Materials* thanks the anonymous reviewers for their contribution to the peer review of this work.

Reprints and permissions information is available at www.nature.com/reprints.